RSC Advances

PAPER

View Article Online
View Journal | View Issue

Check for updates

Cite this: *RSC Adv.*, 2025, **15**, 49455

Open Access Article. Published on 11 December 2025. Downloaded on 4/30/2026 6:26:57 AM. This article is licensed under a Creative Commons Attribution-NonCommercial 3.0 Unported Licence.

Unveiling the mechanism of the electroreduction of CO_2 to CO over ZIF-8, ZIF-67, and ZIF-90: a DFT perspective

Imtiaz Hussain, [a] Umar Farooq [a] and Khurshid Ayub *[b]

Received 27th July 2025
Accepted 23rd November 2025

DOI: 10.1039/d5ra05431a

rsc.li/rsc-advances

The carbon dioxide reduction reaction (CO_2RR) is an important solution for reducing carbon levels. Achieving high selectivity and low cost for the catalyst are the main challenges. In this study, computational approaches at the density functional theory (DFT) level are employed to investigate the catalytic activity and mechanism of the conversion of CO_2 to CO by zeolitic imidazolate framework (ZIF)-based catalysts (ZIF-8, ZIF-67, ZIF-90). Analysis of the activation energy (E_a) barrier reveals that ZIF-8 is the most efficient ($E_a = 0.39$ eV) among the considered catalysts. The quantum theory of atoms in molecules (QTAIM) and noncovalent interaction index (NCI) analyses during the activation step of the CO_2 molecule reveal the partial covalent and strong electrostatic interactions between the analyte (CO_2 molecule) and the catalysts (ZIF-8, ZIF-67, and ZIF-90) at various sites. The natural bonding orbitals (NBO) and electron density difference (EDD) analyses confirm the charge redistribution and bending of the CO_2 molecule as it interacts with the catalyst surface during the activation step. Overall, the study's findings indicate ZIF-8 to be the most stable and effective electrocatalyst surface for the CO_2RR.

1. Introduction

The consumption of fossil fuels, *viz.*, coal, natural gas, and petroleum, has led to a gradual increase in CO_2 emissions, leading to disasters such as global warming,[1,2] flooding, droughts, and heat waves.[3–7] Since the start of the 21st century, the CO_2 emission rate has been increasing at ≈3% per year.[8] To achieve the goal of net-zero CO_2 emissions (reducing by 80–95% by 2050[9,10]), many chemical efforts are being introduced to overcome the problem *via* thermal catalysis,[11,12] photocatalysis,[13,14] and chemical catalysis.[15] The electrochemical conversion of CO_2 into value-added chemicals such as CO, CH_4, CH_3OH, HCOOH, and C_2H_5OH has been employed as an eco-friendly method.[16–22] The direct conversion of CO_2 to CO demonstrates significant promise, as it involves only two electron transfer steps along with proton transfer.[23] The as-made CO can be further reduced by the Fischer–Tropsch process[24] to value-added hydrocarbons (C1 and C2 products) and their oxygen derivatives.

As CO_2 is inert under most conditions, the electrochemical CO_2RR is thermodynamically and kinetically unable to activate C=O bonds, hindering the formation of C–C and C–H bonds.[25–29] The CO_2RR process also suffers from drawbacks, such as poor selectivity toward the target products, inferior catalytic activity, and low energy. It demands the development of efficient electrocatalysts. Many efforts have been devoted to the electrochemical catalysts for the CO_2RR, including metals,[30–32] metal alloys,[33–35] oxides,[36,37] and chalcogenides[38,39] of transition metals, carbon-based materials,[40–42] and single-atom catalysts (SACs).[43–45] The noble metals, including Ag, Au, Cu, and Pd, demonstrate outstanding efficacy in the electrocatalytic conversion of CO_2 to CO.[46–54] Nonetheless, the limitations of these catalysts, including scarcity, elevated costs, and susceptibility to poisoning, significantly hinder their widespread commercial utilization.

Recently, heteroatom-doped carbon materials have emerged as effective catalysts for the electrochemical CO_2RR.[42,55–58] Particularly, new carbon catalysts doped with atomic metals have garnered a great deal of interest due to their effective electrochemical reduction of CO_2 to CO.[42,59–62] Metal–organic frameworks (MOFs), porous materials consisting of metal and organic linkers, have superb capability for CO_2 capture and conversion due to their tunable bandgap, adjustable pore size, well-defined crystalline structure, and large specific surface area.[63–65]

Among the various MOFs, ZIFs exhibit superior CO_2RR selectivity toward CO. This CO is used for coupling to form C–C, which is necessary for obtaining multi-carbon value-added products.[66–68] ZIF-8, ZIF-67, and ZIF-90 were selected for this study due to their electrocatalytic performance, high surface area and porosity, chemical stability, and selective CO_2 adsorption. ZIF-8—which consists of Zn^{2+} linked to 2-methylimidazole (2-mIm) through N moieties in a quadrilateral geometry—exhibits superior electrochemical CO_2RR activity

[a]School of Chemistry, University of the Punjab, Lahore, Pakistan

[b]Department of Chemistry, COMSATS University Islamabad, Abbottabad Campus, KPK, 22060, Pakistan. E-mail: khurshid@cuiatd.edu.pk; Fax: +0092 992 383591-5

© 2025 The Author(s). Published by the Royal Society of Chemistry

Open Access Article. Published on 11 December 2025. Downloaded on 4/30/2026 6:26:57 AM. This article is licensed under a Creative Commons Attribution-NonCommercial 3.0 Unported Licence.

among the ZIF family.[69–71] ZIF-67, which consists of Co^{2+} linked to 2-mIm by N moieties in a quadrilateral geometry, has wide applications in various fields, including catalysis.[72] ZIF-90, which consists of Zn^{2+} linked to imidazole-2-carboxyaldehyde (ICA), has wider applications in catalysis, drug delivery, *etc.*[73]

Density functional theory (DFT) simulations are considered to be one of the most efficient and advanced tools for theoretical exploration of the pathways of catalysis.[74–76] Here, to explore the mystery of the electronic properties of the reactants, products, and intermediates involved, and the pathway of the CO_2RR to give CO, a DFT-based comparative study of structurally related ZIFs (ZIF-8, ZIF-67, and ZIF-90) is performed. The aim of the study is to find an efficient and a more-selective electrocatalyst for the CO_2RR. We have explored the energetics and the stabilities of various species involved in the conversion of CO_2 to CO. The electronic properties and interactions of the analyte, the catalyst, and the intermediates are characterized using frontier molecular orbitals (FMO), natural bonding orbitals (NBO) charge, electron density differences (EDD), noncovalent index interactions (NCI), and quantum theory of atoms in molecules (QTAIM) analyses. This mechanistic study will enable us to design and understand more efficient catalysts for CO_2RR.

2. Computational methodology

The Gaussian 09®[77] program package was used for DFT calculations. The B3LYP functional with the 6-31G(d,p) basis set was used during geometry optimizations for all non-metallic elements (C, H, O, and N), while the B3LYP/SDD (Stuttgart–Dresden effective core potential) basis set was employed for the Zn and Co atoms. The SDD basis set has been widely used and validated for describing the electronic structure and coordination environment of transition metals in metal–organic frameworks and related catalytic systems. Its use ensures a reliable balance between computational efficiency and accuracy in modeling metal–ligand interactions. The hybrid DFT functional B3LYP is well known for its ability to calculate the thermodynamic parameters and electronic properties of compounds in a quantum-chemical manner.[78–80] It is frequently adopted for both geometry optimizations and mechanistic studies as a reliable functional.[81–83] For structure visualization, GaussView® (version 5), Visual Molecular Dynamics® (VMD), Multiwfn package® (version 3.8) and Chemcraft® packages were used.[84–86]

Vibrational frequency analysis was performed for all states at the DFT-optimized geometries to confirm the stationary points as true minima or transition states as saddle points. True minima were confirmed by the absence of imaginary frequencies, while transition states were characterized by a single imaginary frequency. Three ZIF-based catalysts (ZIF-8, ZIF-67, and ZIF-90) were employed in the mechanistic investigation of the CO_2 reduction reaction (CO_2RR) after being optimized based on their experimentally available structural data. Various spin states were considered for geometry optimization to obtain the most stable spin state (Table S1).

The adsorption energy (E_{ads}) of a species is the amount of energy released when it is adsorbed on a surface or that is required for it to desorb from that surface. Eqn (1) is used to determine the energy for CO_2 adsorption (E_{ads}) over various catalysts, where $E_{CO_2@Cat}$ stands for the electronic energy of the CO_2 adsorbed on the catalyst, E_{CO_2} for the electronic energy of a single CO_2 molecule, and E_{Cat} for the electronic energy of the specified catalyst.

$$E_{ads} = E_{CO_2@Cat} - (E_{Cat} + E_{CO_2}) \tag{1}$$

Eqn (2) provides the activation energy (E_a), where E_{TS} and E_R are energies of the transition state and reactants, respectively.

$$E_a = E_{TS} - E_R \tag{2}$$

The reaction energy (E_r) corresponds to the heat released or absorbed during a reaction. It helps to find whether a reaction is endothermic (+ve value of E_r) or exothermic (−ve value of E_r) and is given by eqn (3).

$$E_r = E_P - E_R \tag{3}$$

where, E_P and E_R are the energies of the products (P) and reactants (R), respectively.

EDD and NBO analyses help evaluate the mechanism of the CO_2RR by the designed complexes by investigating the nature of donor–acceptor interactions. To explain the nature of the bonding in terms of orbital interaction and charge transfer, NBO analysis was performed at B3LYP/6-31G(d,p) level of theory. Additionally, topological studies such as QTAIM and NCI were carried out using the Multiwfn package (version 3.8) for a better understanding of the nature of interatomic interactions.

3. Results and discussion

3.1. Geometry optimization of catalysts

The geometries of the designated catalysts (ZIF-8, ZIF-67, and ZIF-90) were optimized by taking their single tetrahedron unit before using them as electrocatalysts in CO_2RR. In the optimized geometries of the catalysts, the linker (2-mIm for ZIF-8 and ZIF-67 and ICA for ZIF-90) surrounds the central metal (Zn for ZIF-8 and ZIF-90 and Co for ZIF-67) tetrahedrally through nitrogen sites (Fig. 1), which is consistent with the literature.[87] The approximate metal–linker (M–L) bond lengths for ZIF-8, ZIF-67, and ZIF-90 are 2.03 Å, 2.01 Å, and 2.06 Å, respectively. These bond lengths are indicative of the strength of the M–L bond and how the linker influences the coordination environment.

To understand the influence of changing the central metal ion (in the case of ZIF-8 and ZIF-67) and linkers (in case of ZIF-8 and ZIF-90) on the electronic properties of the catalysts, FMO analysis of the designed catalysts was performed (Fig. 2). The analysis showed that the gap between the highest occupied molecular orbital (HOMO) and the lowest unoccupied molecular orbital (LUMO) is increased by changing the metal from Zn in ZIF-8 to Co in ZIF-67, whereas this gap is reduced by changing the linkers from 2-mIm in ZIF-8 to ICA in ZIF-90. The HOMO–LUMO gap for ZIF-8, ZIF-67, and ZIF-90 is 6.50 eV, 6.56 eV, and 4.77 eV, respectively. In the case of ZIF-67, its

 © 2025 The Author(s). Published by the Royal Society of Chemistry

Open Access Article. Published on 11 December 2025. Downloaded on 4/30/2026 6:26:57 AM.
This article is licensed under a Creative Commons Attribution-NonCommercial 3.0 Unported Licence.

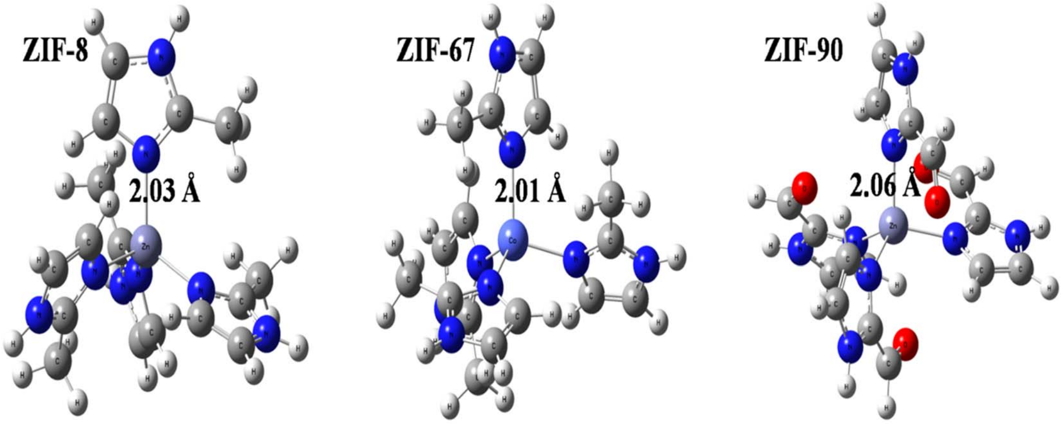

Fig. 1 Optimized geometries of ZIF-8, ZIF-67, and ZIF-90 with the M–L bond lengths (through nitrogen sites) determined at the B3LYP/6-31G(d,p) (H, C, N, and O) and SDD (Zn and Co) levels of theory.

stronger M–L bonding, compared with that of ZIF-8, leads to stabilization of the HOMO and destabilization of the LUMO, and increases the gap between them. In the case of ZIF-90, the electron-withdrawing formyl/aldehyde group adds new unoccupied orbitals of low energy and reduces electron density at the linker side, resulting in a reduced HOMO–LUMO gap. The energy values of the HOMO, LUMO and HOMO–LUMO energy gap for ZIF-8, ZIF-67, and ZIF-90 are listed in Table S2.

3.2. ZIF-catalyzed mechanism for the CO_2RR

To investigate the mechanism of the CO_2RR to give CO,[88,89] the geometries of the transition states and intermediates were studied. Initially, the CO_2 molecule is weakly physisorbed on the surface of the catalyst, resulting in the formation of a van der Waals complex consisting of a tetrahedral unit of the catalyst and a linear CO_2 molecule. During this step, the CO_2 molecule orients towards the active site on the catalyst before the activation step. This does not affect the geometries of either of the reactants relative to their free states. The next step is the activation of CO_2 by the electrocatalyst, yielding ZIF–COO^- as an intermediate. This step is followed by the first protonation step, which produces ZIF–COOH. Finally, the second protonation, accompanied by electron transfer, leads to the formation of water gas (CO and H_2O), which immediately desorbs from the catalyst surface.[90] This is due to the polarity of CO, as its negatively charged C atom does not remain bonded to the C atom of the linker, which is also an electron donor site of the electrocatalyst. To evaluate the catalytic performance for the reduction of CO_2 to CO, the energy barrier for the activation step was studied. The activation energy or energy barrier (E_a) values for CO_2 using ZIF-8, ZIF-67, and ZIF-90 are listed in Table S3.

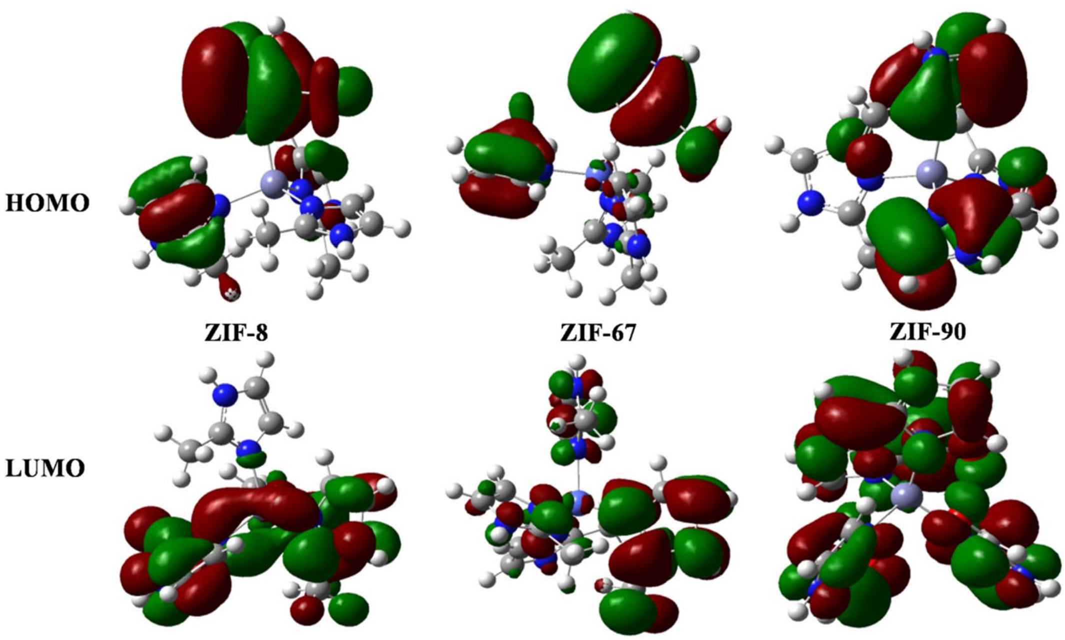

Fig. 2 HOMO–LUMO isosurfaces for ZIF-8, ZIF-67, and ZIF-90.

Open Access Article. Published on 11 December 2025. Downloaded on 4/30/2026 6:26:57 AM. This article is licensed under a Creative Commons Attribution-NonCommercial 3.0 Unported Licence.

3.3. Mechanism of the CO_2RR catalyzed by ZIF-8

The energy diagram of the DFT-based mechanistic study of the CO_2RR catalyzed by ZIF-8 is shown in Fig. S1. Initially, the reactant CO_2 is physiosorbed at the surface of the catalyst, forming a van der Waals complex (**vdW**) comprising a tetrahedral unit of ZIF-8 and a linear CO_2 molecule with a relative energy of −0.27 eV with respect to the energy of the reactants in their free states. In this step, the reactants are properly oriented toward each other and are stabilized relative to their free states by 0.27 eV before activation of the CO_2 molecule for the CO_2RR. Electron transfer then occurs to form a complex (**Int1**) comprising the ZIF-8, CO_2, and an electron with an electron affinity value of 5.27 eV. This leads to the activation of the CO_2 molecule, which results in the formation of a ZIF8–COO^- intermediate (**Int2**) by passing through the transition state **TS**. In **TS**, CO_2 interacts with the catalyst through its C atom at the sp^2-hybridized C atom of the linker and is then chemisorbed at the catalyst to give **Int2.**[91] The formation of **TS** with a relative energy of −5.06 eV must overcome an activation energy barrier of 0.48 eV (11.07 kcal mol^{-1}) to give **Int2** with a relative energy of −5.61 eV. The structural parameters, such as vibrational frequencies, bond lengths and bond angles, of the reacting species are critical in the activation step, which demonstrate the stability of the transition state and in turn facilitate protonation. In the case of ZIF-8, the C=O bond lengths of the CO_2 molecule extend from 1.17 Å in **Int1** to 1.27 Å and 1.21 Å in **TS** and finally to 1.29 Å and 1.22 Å in **Int2**. During this activation, the C–C bond distance between the interacting carbon atoms of CO_2 and the linker is reduced to 2.18 Å in **TS** and 1.58 Å in **Int2**, from a distance of 3.39 Å in **Int1** (Fig. S1). The O–C–O bond angle also changes from 180° in **Int1** to 135° in **TS** and finally becomes 128° in **Int2**. The L–M–L bond angle also increases to accommodate the attachment of CO_2. In the gas phase, CO_2 shows two main vibrational modes, asymmetric stretching at 2436 cm^{-1} and symmetric stretching at 1372 cm^{-1}. During the activation step, the frequencies of these modes decrease, indicating bending of the CO_2 molecules and weakening of the carbon–oxygen double bonds. The asymmetric stretching frequency changes from 2436 cm^{-1} in the gas phase to 1788 cm^{-1} in **Int1**, 1873 cm^{-1} in **TS**, and 1805 cm^{-1} in **Int2**. This elongation of the C=O bond lengths, reduction in the C–C bond distance, and bending of the CO_2 molecule upon adsorption, as evident from the bond angle reduction and reduction in vibrational frequencies of the C=O bond, confirm the activation of the CO_2 molecule over the ZIF-8. This activation step leads to the formation of **Int2**, releasing 0.17 eV of energy overall in this step. In the next step, the first protonation occurs, giving the ZIF8–COOH intermediate (**Int3**) with a relative energy of −14.69 eV. The stability of intermediate **Int3** is evident by the release of 9.08 eV as proton affinity energy and is in accordance with the value found by Lias *et al.*[92] **Int3** undergoes decarboxylation upon the second protonation, accompanied by the addition of an electron to give a product complex comprising ZIF-8 and water gas, *i.e.*, CO and H_2O, with a relative energy of −15.72 eV. During this decarboxylation step, 1.03 eV of energy is released, as supported by the study of Hu *et al.* on the decarboxylation mechanism in the gas phase.[93] The enthalpy of the product complex indicates that it is more stable than the reactants.

To ensure that the located transition states truly connect the desired reactants and products, intrinsic reaction coordinate (IRC) calculations were performed for a representative case: the CO_2 activation step on ZIF-8. The IRC analysis was carried out using the B3LYP/SDD (for Zn) and 6-31G(d,p) (for non-metal atoms) level of theory. The successful IRC path confirms that the optimized transition state for CO_2 activation over ZIF-8 is a true first-order saddle point connecting the correct reactant and product minima. Based on this representative validation, the same TS optimization protocol was applied to other catalysts (ZIF-67 and ZIF-90).

3.4. Mechanism of the CO_2RR catalyzed by ZIF-67

The energy diagram of the DFT-based mechanistic study of the CO_2RR catalyzed by ZIF-67 is shown in Fig. S2. In this case, the van der Waals complex (**vdW′**) comprising the tetrahedral unit of ZIF-67 and linear CO_2 molecule is formed with a relative energy of −0.11 eV. Following the addition of an electron, an intermediate (**Int1′**) comprising ZIF-67 and CO_2 is formed, with an electron affinity of 6.59 eV. The intermediate ZIF-67–COO^- (**Int2′**) is then formed, resulting in the activation of the CO_2 molecule by passing through a transition state (**TS′**). Here, CO_2 interacts through its C atom with the ZIF-67 at the sp^2-hybridized C atom of 2-mIm. The formation of **TS′** with a relative energy of −5.40 eV must overcome an activation energy barrier of 1.30 eV (29.98 kcal mol^{-1}) to form **Int2′** with a relative energy of −5.75 eV. In the case of ZIF-67, the C=O bond lengths of the CO_2 molecule extend from 1.17 Å in **Int1′** to 1.23 Å and 1.20 Å in **TS′** and finally to 1.30 Å and 1.22 Å in **Int2′**. During this activation, the C–C bond distance between the carbon atom of CO_2 and that of the linker is reduced from 4.46 Å in **Int1′** to 2.18 Å in **TS′** and 1.57 Å in **Int2′** (Fig. S2). The O–C–O bond angle changes from 180° in **Int1′** to 143° in **TS′** and finally becomes 128° in **Int2′**. The L–M–L bond angle also increases to accommodate the attachment of CO_2. Frequency analysis of the activation step revealed a redshift in the values of the CO_2 molecule, indicating its bending and weakening of its carbon–oxygen bonds. The asymmetric stretching frequency of CO_2 changes from 2436 cm^{-1} in the gas phase to 2427 cm^{-1} in **Int1**, 1996 cm^{-1} in **TS**, and 1788 cm^{-1} in **Int2.** These changes confirm the activation of the CO_2 molecule over ZIF-67. This activation step leads to the formation of **Int2′** with the absorption of an energy of 0.50 eV. In the next step, the first protonation occurs, giving a ZIF67–COOH intermediate (**Int3′**) with a relative energy of −14.42 eV. The stability of intermediate **Int3′** is evident from the release of 8.67 eV as proton affinity energy.[92] **Int3′** undergoes decarboxylation upon the second protonation, accompanied by the addition of an electron, giving a product complex comprising ZIF-67 and water gas, *i.e.* CO and H_2O, with a relative energy of −16.23 eV.

3.5. Mechanism of the CO_2RR catalyzed by ZIF-90

The energy diagram of the DFT-based mechanistic study of the CO_2RR catalyzed by ZIF-90 is shown in Fig. S3. For ZIF-90, the

 © 2025 The Author(s). Published by the Royal Society of Chemistry

Open Access Article. Published on 11 December 2025. Downloaded on 4/30/2026 6:26:57 AM. This article is licensed under a Creative Commons Attribution-NonCommercial 3.0 Unported Licence.

van der Waals complex (**vdW″**) is formed and stabilized with a relative energy of −0.40 eV. The activation of the CO_2 molecule is initiated by the addition of an electron to give a complex (**Int1″**) including ZIF-90, CO_2 and an electron with an electron affinity of 6.53 eV. The activation of the CO_2 molecule results in the formation of the ZIF90–COO$^-$ intermediate (**Int2″**) by passing through a transition state (**TS″**). CO_2 interacts through its C atom with the sp^2-hybridized C atom of the ICA in the ZIF-90. The formation of **TS″** with a relative energy of −5.42 eV must overcome an activation energy barrier of 1.51 eV (34.82 kcal mol^{-1}) to give **Int2″** with a relative energy of −5.52 eV. In the case of ZIF-90, the C═O bond lengths of the CO_2 molecule extend from 1.17 Å in **Int1″** to 1.23 Å and 1.20 Å in **TS″** and finally become 1.28 Å and 1.22 Å in **Int2″**. During this activation, the C–C bond distance between the interacting carbon atoms of CO_2 and the linker is reduced to 1.90 Å in **TS″** and 1.61 Å in **Int2″**, from a distance of 4.05 Å in **Int1″** (Fig. S3). The O–C–O bond angle changes from 180° in **Int1″** to 142° in **TS″** and finally becomes 131° in **Int2″**. The L–M–L bond angle also increases to accommodate the attachment of CO_2. Frequency analysis of the activation step revealed a redshift for CO_2, which indicated its bending and weakening of its carbon–oxygen bonds. The asymmetric stretching frequency of CO_2 changes from 2436 cm^{-1} in the gas phase to 2433 cm^{-1} in **Int1**, 1999 cm^{-1} in **TS**, and 1829 cm^{-1} in **Int2**. These changes indicate the activation of the CO_2 molecule over the ZIF-90. This activation step leads to the formation of **Int2″** by absorbing an energy of 1.41 eV overall in this step. In the next step, the first protonation occurs, giving a ZIF90–COOH intermediate (**Int3″**) with a relative energy of −14.04 eV. The stability of intermediate **Int3″** is evident by the release of 8.52 eV as proton affinity energy.[92] **Int3″** undergoes decarboxylation upon second protonation, accompanied by the addition of an electron, giving a product complex comprising ZIF-90 and water gas, *i.e.*, CO and H_2O, with a relative energy of −16.39 eV.

3.6. Effect of solvent

To evaluate the solvent effect on the energetics of the reaction mechanism, single-point SMD calculations of the involved intermediates and transition states were performed using water as a solvent. This systematically modified the energetics of the intermediates, but did not alter the sequence of the mechanism observed in the gas phase.

Transition states for all catalysts were stabilized by the addition of the solvent effect, as evident from the lowering of their activation barriers. In the cases of ZIF-8, ZIF-67, and ZIF-90, E_a changes from 0.48 eV, 1.30 eV, and 1.51 eV to 0.11 eV, 0.83 eV, and 0.95 eV, with the activation barriers being lowered by 0.37 V, 0.47 V and 0.56 V, respectively.

The solvent stabilization of the transition state structures (**TS**) implies that transition states with a polar nature will be more stabilized in the aqueous environment of the electrochemical experiment, thus lowering the kinetic barriers for the reaction to occur. The solvent causes some intermediates like **Int3** to gain a significant amount of stability (for instance, ZIF-8 **Int3**: −9.08 → −12.98 eV), which hints that polar/charged species are intensively solvated. Conversely, the very early intermediates (**Int1** to be exact) are the least stabilized by solvation in the case of ZIF-8 (ZIF-8 **Int1**: −5.27 → −1.75 eV), which implies that the effects caused by solvation are relatively dependent on the charge distribution and shape of each species.

While the energies were altered in absolute terms, the relative positions of the intermediates and the identity of the probable rate-determining step remained nearly the same in qualitative terms in both the gas and implicit-solvent data. A good example is the situation in which the energies of all the **TS**s decrease, but ZIF-90 retains the highest **TS** energy (0.95 eV) among the three in the SMD calculations, which is in line with the gas-phase trend.

The net effect of solvation is the lowering of the activation barriers, which is seen as additional stabilization of the polar intermediates; this is in line with lower overpotentials and changed selectivity in aqueous electrochemical cells, which are consistent with the experimental observations. Thus, the gas-phase investigation gives a mechanistic view, and the SMD results indicate that solvent inclusion changes the specific barrier heights but not the proposed mechanism.

3.7. Comparison of catalytic activity

The activation energy barriers for the CO_2RR over the proposed catalysts are between 0.48 and 1.51 eV, as shown in Table S3. Overall, ZIF-8 exhibits the lowest activation energy barrier among the catalysts considered in this study (0.39 eV), which can be readily overcome under mild conditions. This low activation barrier for ZIF-8, as compared to the other ZIFs, can be explained by comparing the geometries of their transition states for the activation step. The geometries of the transition state for the CO_2 reduction reaction over ZIF-8, ZIF-67, and ZIF-90 are quite complex and differ from each other in accordance with their respective activation barriers. In the frequency analyses of the respective species, a progressive redshift is observed in the asymmetric stretching mode from the reactant (**Int1**) *via* the transition state (**TS**) and the intermediate (**Int2**). This confirms the stepwise activation and the gradual bending of CO_2. ZIF-8 shows the strongest frequency reduction among all the studied catalysts; this is an indication of stronger catalyst –CO_2 interaction and more effective activation (Table S4). A correlation exists between this trend and the higher catalytic activity of ZIF-8 that has been reported experimentally for CO_2 reduction reactions. In the transition state of ZIF-8, the bond lengths of C═O are 1.27 Å and 1.21 Å, which are greater than that of 1.17 Å in free CO_2 and suggest a great deal of charge transfer from the catalyst to CO_2. In contrast, the ZIF-67 and ZIF-90 transition states have less pronounced C═O elongation with distances of 1.23 Å and 1.20 Å, respectively, which indicates lower charge transfer. Another critical factor influencing activation is the O–C–O bond angle; its significant reduction to 135° in the case of ZIF-8 strongly favors CO_2 activation. For ZIF-67 and ZIF-90, the angles are greater than those for ZIF-8, being 143° and 142°, respectively, indicating reduced bending of CO_2 and therefore weaker activation. The C–C bond length between

Open Access Article. Published on 11 December 2025. Downloaded on 4/30/2026 6:26:57 AM. This article is licensed under a Creative Commons Attribution-NonCommercial 3.0 Unported Licence.

carbon dioxide and the sp^2-hybrid carbon of the linker also offers insight regarding the interaction strength. Shorter bond lengths indicate stronger interactions and more-efficient charge transfer. ZIF-90 possesses a shorter C–C distance (1.90 Å) than ZIF-8 (2.18 Å) and ZIF-67 (2.18 Å). However, ZIF-90 has the highest activation barrier of 1.51 eV due to the lack of charge transfer from the imidazole-2-carboxaldehyde linker, which is poor at transition state stabilization because of its lower effectiveness. The trend in the observed activation barriers (ZIF-8 < ZIF-67 < ZIF-90) is a result of the CO_2 distortion, linking strength, and charge transfer from the complex. Regarding these ZIFs, ZIF-8 has the most changeable transition state shape, thus leading to the smallest amount of energy being needed for activation. This indicates that, in comparison to the other catalysts under study, ZIF-8 is the best candidate for the CO_2RR because it offers the most favorable transition state geometry together with the lowest energy needed for activation.

Our DFT study, which revealed the mechanistic trends, showed a strong relationship to the experimentally observed CO_2R activity and selectivity in ZIF-based catalysts. Specifically, the extent of CO_2 activation (indicated by the ν_3 reduction in the frequencies of IR modes, charge transfer, and transition state stabilization) correlates with higher CO selectivity and lower overpotential in the experimental data. Compared to those obtained using Ag,[94] Cu and Cu_2O,[95] and Pd_3Au[96] surfaces as the electrocatalyst for the CO_2RR, the computed CO_2RR barrier for ZIF-8 is substantially smaller. ZIF-8 is a potential catalyst for the CO_2RR owing to its highest activity among all catalysts studied here.

3.8. QTAIM and NCI analyses

The nature of the interactions between the analyte and the catalyst was analyzed using a topological analysis, quantum theory of atoms in molecules (QTAIM). The values of the topological parameters, *viz.*, the electron density (ρ), Laplacian of electron density ($\nabla^2\rho$), sum of electron densities (H), kinetic energy (G), potential energy (V), and interaction energy (E_{int}) of individual bonds, were used to gain deep insight into the nature of interactions. Values of ρ less than 0.1 a.u. indicate the presence of weak interactions (for van der Waals <0.02 a.u., for partially covalent 0.02–0.2 a.u.), whereas values greater than 0.2 a.u. represent strong covalent interactions. Positive values of $\nabla^2\rho$ and H represent noncovalent interactions, whereas negative values indicate covalent interactions. Values of E_{int} less negative than -3 kcal mol^{-1} for individual bonds represent weak interactions such as van der Waals forces; values of -3 to -10 kcal mol^{-1} represent strong electrostatic interactions like hydrogen bonding, and values more negative than -10 kcal mol^{-1} represent strong interactions, for example, covalent bond values are -50 kcal mol^{-1} or more negative.[84,97] The E_{int} of individual bonds was calculated by using eqn (4).

$$E_{\text{int}} = V/2 \tag{4}$$

The ratio $-V/G$ is another parameter that indicates the nature of interactions. It should be less than 1 a.u. for noncovalent interactions and 1–2 a.u. for partially covalent interactions. At bond critical points (BCPs), the values of G and V remain positive and negative, respectively. The QTAIM analysis results for intermediate and transition states are given in Table S5, whereas BCPs are shown in Fig. 3.

Through QTAIM analysis, 3 and 5 BCPs were seen for **Int1** and **TS** on the ZIF-8 surface, 4 and 5 BCPs were discovered for **Int1′** and **TS′** on the ZIF-67 surface, and 3 and 4 BCPs were discovered for **Int1″** and **TS″** on the ZIF-90 surface. An increase in the number of BCPs for the respective transition states relative to that of intermediates for each catalytic surface

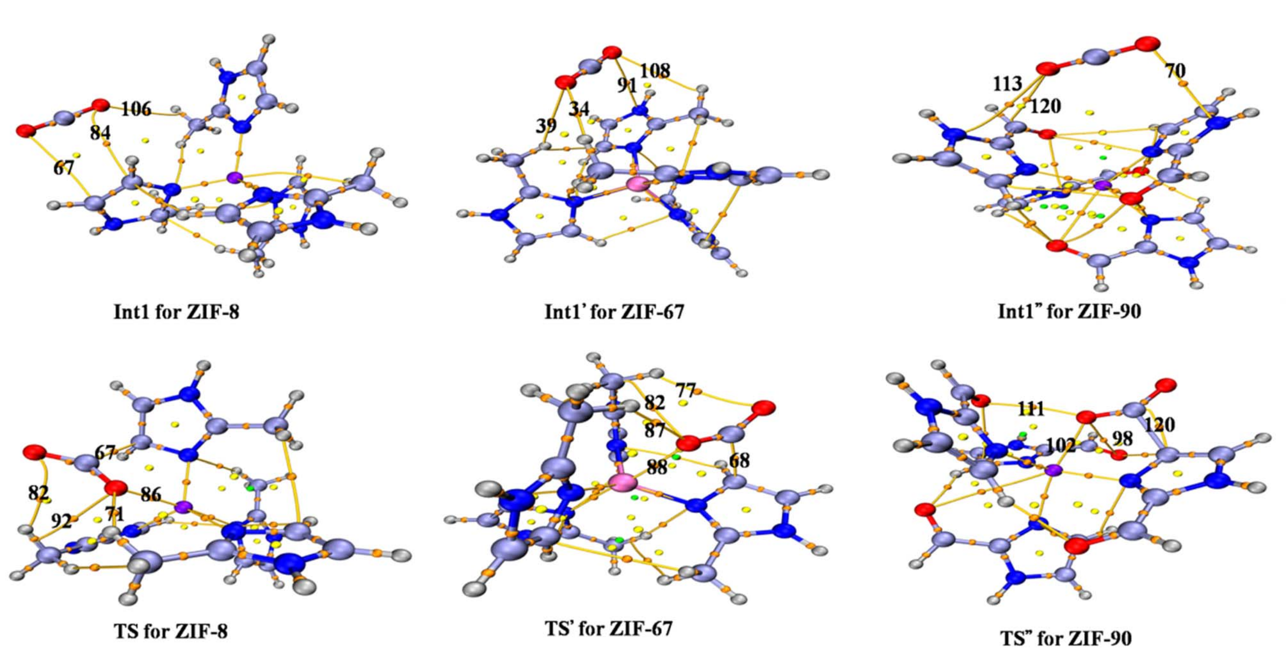

Fig. 3 QTAIM analysis results of respective intermediates and transition states for ZIF-8, ZIF-67, and ZIF-90.

 © 2025 The Author(s). Published by the Royal Society of Chemistry

Open Access Article. Published on 11 December 2025. Downloaded on 4/30/2026 6:26:57 AM.
This article is licensed under a Creative Commons Attribution-NonCommercial 3.0 Unported Licence.

indicates the stabilization of the transition state relative to the reactants. At all the BCPs of the intermediates (**Int1**, **Int1′** and **Int1″**), the values of ρ and $-V/G$ are less than 0.02 and 1, respectively (Table S5). The values of H and $\nabla^2\rho$ are positive, and the values of E_{int} are less negative than -3 kcal mol^{-1}. These values of the structural parameters indicate the presence of weak noncovalent interactions such as van der Waals interactions. In the **TS** for ZIF-8, at the BCPs C50–C14 and O51–Zn32, the values of all these parameters are in ranges indicating partially covalent interactions, while at the BCP O51–H40, the value of E_{int} is -5.648 kcal mol^{-1}, suggesting the presence of hydrogen bonding. In the **TS′** for ZIF-67, at two BCPs, C49–C14 and O50–Co52, the values of all these parameters indicate partially covalent interaction, while at the BCP O50–H39, the value of E_{int} is -4.706 kcal mol^{-1}, indicating the presence of hydrogen bonding. In the **TS″** for ZIF-90, at the two BCPs, C46–C3 and O47–Zn1, the values of all these structural parameters are in the range suggesting partial covalent interaction. These QTAIM parameters at the remaining BCPs for the TS indicate noncovalent interactions.

QTAIM analysis of the transition states for ZIF-8, ZIF-67, and ZIF-90 confirmed a distinct trend concerning stability. ZIF-8 has the electron density (ρ) at the bond critical points (BCPs), with 0.062 a.u. for C50–C14 and 0.055 a.u. for O51–Zn32, indicating the strongest bonding interactions. ZIF-67 comes next with moderate values of 0.052 a.u. for C49–C14 and 0.038 a.u. for O50–Co52, while ZIF-90 shows the weakest interactions of 0.038 a.u. for O47–Zn1 and 0.022 a.u. for C46–C3. Similarly, the most negative value of potential energy density (V), which indicates the level of bond stabilization, was recorded for ZIF-8 (-0.050 a.u. for C50–C14 and -0.108 a.u. for O51–Zn32), ZIF-67 (-0.036 a.u. for C49–C14 and -0.074 a.u. for O50–Co52) and the least negative value for ZIF-90 (-0.050 a.u. for C46–C3 and -0.064 a.u. for O47–Zn1). The interaction energy ($E_{\mathrm{int}} = V/2$) shows the same trend, with ZIF-8 having the most stabilizing values (-15.688 kcal mol^{-1} for C50–C14 and -33.885 kcal mol^{-1} for O51–Zn32), followed by ZIF-67 (-11.295 kcal mol^{-1} for C49–C14 and -23.218 kcal mol^{-1} for O50–Co52), and ZIF-90 having the least stabilizing interactions (-15.688 kcal mol^{-1} for C46–C3 and -20.080 kcal mol^{-1} for O47–Zn1). The bond character ratio ($-(V/G)$) supports this, with ZIF-8 demonstrating the highest values that show strong to partially covalent bonding, ZIF-67 showing some covalent and ionic character, and ZIF-90 showing more closed-shell bonding interactions.

The reason that ZIF-8 has a comparatively higher transition state stability than ZIF-67 and ZIF-90 can be explained by considering the bonding interactions. ZIF-8 has a higher electron density, more negative potential energy density, and larger interaction energy, suggesting greater charge transfer efficiency, which yields a more stable transition state. The cobalt in ZIF-67 tends to alter the electronic environment, weakening the interactions a bit compared to those in ZIF-8, hence its moderate stability. Comparatively, ZIF-90 has the least amount of those bonds because of the presence of ICA, which decreases charge transfer efficiency and stablilizes bonds, which in turn explains the observed progression towards weaker transition state stability: that of ZIF-8 is greater than ZIF-67, which is greater than ZIF-90, where ZIF-8 is most favorable for CO_2 activation, and ZIF-90 is the least stable.

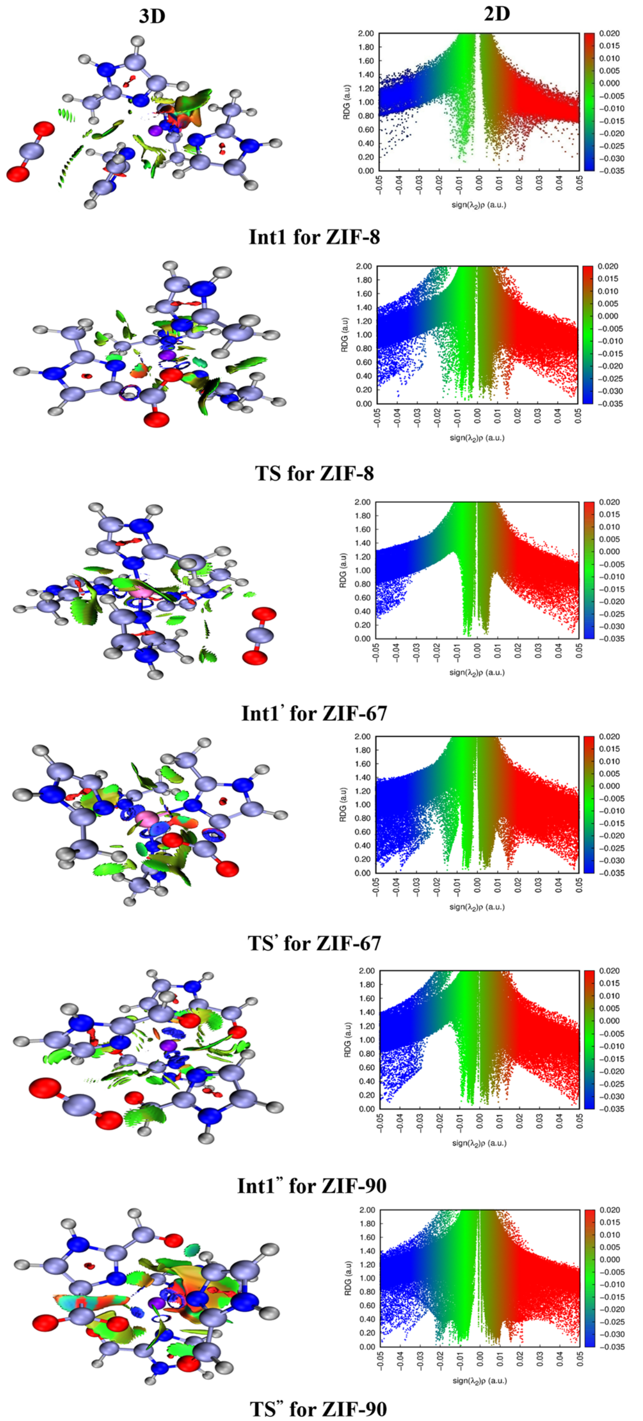

Fig. 4 NCI isosurfaces of the transition states and intermediates for ZIF-8, ZIF-67, and ZIF-90.

Noncovalent interaction index (NCI) analysis is another tool for studying the nature of the different attractive as well as repulsive interactions, *viz.*, H-bonding, weak van der Waals interactions, and steric repulsion interactions between an analyte and catalyst. It assists in finding the stability and

Open Access Article. Published on 11 December 2025. Downloaded on 4/30/2026 6:26:57 AM.
This article is licensed under a Creative Commons Attribution-NonCommercial 3.0 Unported Licence.

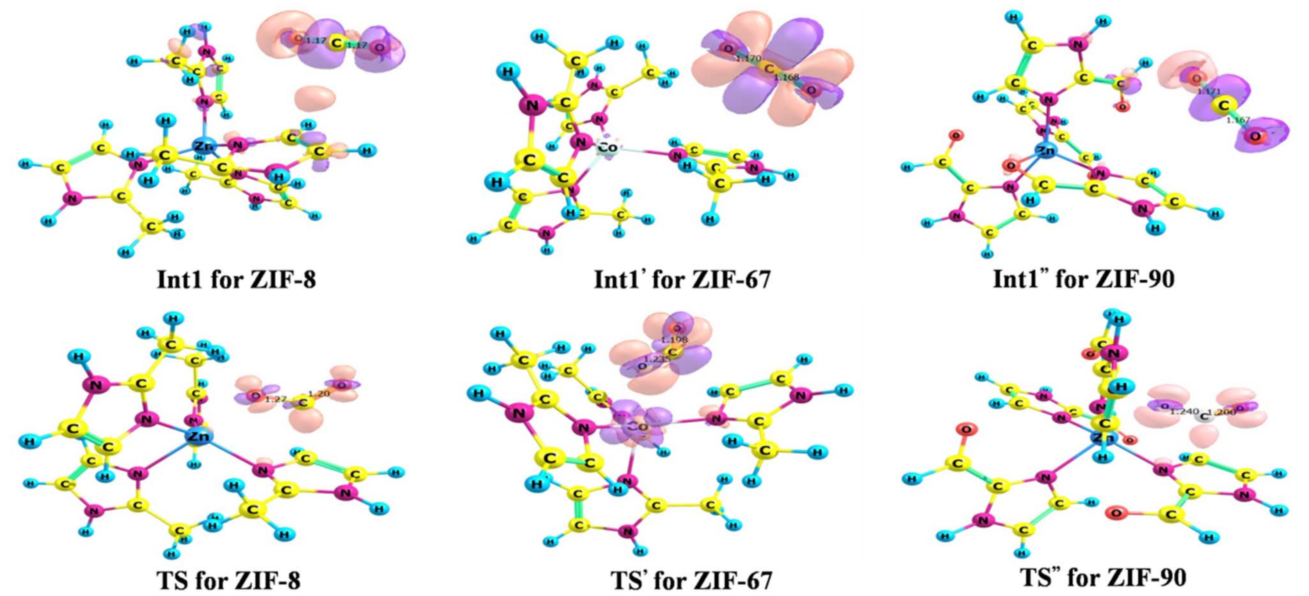

Fig. 5 EDD analysis showing the bending of the CO_2 molecule, C–O bond elongation, and charge redistribution upon moving from the first intermediate to the transition state for ZIF-8, ZIF-67, and ZIF-90.

reactivity of the transition states and intermediates of interest. The NCI analysis is based on the reduced density gradient (RDG) maps (2D and 3D).[98,99] These RDG maps and isosurfaces are further based on ρ and $\nabla^2\rho$ values, as shown in eqn (5).

$$\mathrm{RDG} = \frac{1}{2(3\pi)^{1/3}}\frac{\nabla^2\rho}{\rho^{3/4}} \tag{5}$$

Both the 2D maps and 3D isosurfaces depend upon the values of sign$(\lambda^2)\rho$. In 2D maps, sign$(\lambda^2)\rho$ is plotted at the abscissa while RDG is plotted at the ordinate. The factors sign(λ^2) and ρ represent the type and strength of interaction, respectively. Positive, slightly negative, and highly negative values of sign$(\lambda^2)\rho$ indicate steric repulsions, weak van der Waals interactions, and strong electrostatic interactions, and appear as red-, green-, and blue-colored areas or patches in the maps, respectively. These RDG maps and isosurfaces of the respective intermediates (**Int1**, **Int1**′ and **Int1**″) and transition states (**TS**, **TS**′ and **TS**″) for ZIF-8, ZIF-67, and ZIF-90 are shown in Fig. 4.

The green patches in the 3D RDG isosurfaces of the intermediates (**Int1**, **Int1**′ and **Int1**″) indicate van der Waals interactions between the interacting moieties of fragments. The appearance of green areas in the 2D RDG maps in the range of 0.002 to −0.018 a.u. indicates weak van der Waals interactions between the fragments. For the transition states, the blue donut-shaped patches in the 3D RDG isosurfaces indicate strong electrostatic interactions, *e.g.* partially covalent interactions and H-bonding, and thick green patches indicate weak van der Waals interactions between the interacting moieties of the fragments. In the 2D RDG maps, the appearance of green areas in the range of 0.002 to −0.018 a.u. correspond to weak van der Waals interactions and the blue areas in the range of −0.018 to −0.050 a.u. indicate the strong electrostatic interactions, *e.g.* H-bonding and partially covalent interactions between interacting moieties of the fragments. This analysis of the isosurfaces indicates the stability of the transition states as compared to the complexes. In case of **TS** for ZIF-8, the strong attractive forces (as shown by the donut-shaped blue patches in Fig. 4) between the carbon atoms of CO_2 and the linker group of the catalyst correspond to the greater charge transfer capability of ZIF-8 and lead to a low activation barrier. This barrier increases in **TS**′ of ZIF-67 compared to that in **TS** of ZIF-8 due to the increased repulsive forces operating (as evident from the red-colored patches in Fig. 4) between O of CO_2 and N atom of the linker group of the catalyst. In the case of ZIF-90, **TS**″ has the highest energy barrier due to the presence of only weak attractive forces (as evident from the cyan colored patch in Fig. 4) between the C atoms of CO_2 and the linker group of the catalyst and increased repulsive interactions.

3.9. Natural bond orbitals (NBO) and electron density differences (EDD) analyses

The activation and reduction of CO_2 over the designed catalysts were further confirmed by natural bond orbitals (NBO) and electron density differences (EDD) analyses. NBO analysis was performed to determine the exact amount of charge transfer from the donor (catalyst) to the acceptor (analyte, *i.e.*, CO_2 molecule). The calculated values of the NBO charges on the corresponding species, *i.e.*, analyte and catalyst, are listed in Table S6. Study of the intermediates (**Int1**, **Int1**′ and **Int1**″) and transition states (**TS**, **TS**′ and **TS**″) in the NBO analysis indicated that the catalyst transfers its charge to the analyte species and activates the CO_2 molecule for its subsequent reduction to CO. In the case of the intermediates, the NBO charges on the catalyst moiety are +1.003, 0.994, and 0.997, while those for the analyte are −0.003, 0.006, and 0.003 for ZIF-8, ZIF-67, and ZIF-90,

 © 2025 The Author(s). Published by the Royal Society of Chemistry

Open Access Article. Published on 11 December 2025. Downloaded on 4/30/2026 6:26:57 AM. This article is licensed under a Creative Commons Attribution-NonCommercial 3.0 Unported Licence.

respectively. In the transition states, the NBO charges on the catalysts are +1.612, 1.387, and 1.354, whereas those on the analytes are −0.612, −0.387, and −0.354 in the case of ZIF-8, ZIF-67, and ZIF-90, respectively. It clearly indicates the charge transfer from the catalyst to the analyte. This charge transfer follows the trend of highest to lowest for ZIF-8, ZIF-67, and ZIF-90, which explains the order of their activation barriers from lowest to highest for CO_2 activation, respectively. The greater the charge transfer from the catalyst to CO_2, the easier its activation and hence the smaller activation barrier will be. Overall, this charge transfer reveals that the catalyst shifts charge to the analyte, assisting the C–O bond elongation and activation of the CO_2 molecule for further reduction to CO.

The electron density difference (EDD) contours for the relevant intermediates and transition states were used to investigate the interaction of CO_2 molecules with the ZIF-8, ZIF-67, and ZIF-90 surfaces. Fig. 5 shows the contours for the interaction of CO_2 on ZIF-8, ZIF-67, and ZIF-90. Purple represents the accumulation of charge, while pink represents the depletion of charge. The contours of the respective intermediates and transition states for each catalyst demonstrate that, upon adsorption of CO_2 on the catalyst surface, the carbon atom of CO_2 interacts with the sp^2-hybridized carbon atom of the corresponding linker, converting its localized π-bond character into a delocalized, resonating form. During this interaction, the CO_2 molecule bends, and both C–O bonds elongate. For ZIF-8, these bonds elongate from 1.17 Å to 1.27 Å and 1.20 Å, for ZIF-67 from 1.170 Å to 1.235 Å and 1.198 Å, and for ZIF-90 from 1.171 Å to 1.200 Å and 1.240 Å. This bending and bond elongation in CO_2 causes the redistribution of the electronic density. It also reveals that the charge is being transferred from the catalyst to the analyte. The EDD results in Fig. 5 agree with the NBO analysis, indicating a strong interaction between the analyte and the catalytic surface.

4. Conclusion

In this study, the catalytic reduction of CO_2 to CO over a selection of ZIFs (ZIF-8, ZIF-67, and ZIF-90) was comprehensively investigated using quantum-chemical DFT investigations. Comparison of the CO_2 activation barriers over these ZIFs indicated that the activation of CO_2 is more thermodynamically favorable over ZIF-8, as indicated by its having the lowest activation barrier (0.48 eV) compared to those for ZIF-67 (1.30 eV) and ZIF-90 (1.51 eV). The better catalytic activity of ZIF-8 is attributed to its better electron transferring capability and stabilization of the carboxylate group produced during activation in comparison to ZIF-67 and ZIF-90. This facilitates the subsequent reduction to CO. QTAIM and NCI analyses were carried out to explore the interactions occurring during the activation step of the CO_2 molecule. These reveal the partially covalent and strong electrostatic interactions at the respective interacting sites of the analyte (CO_2 molecule) and the catalyst (ZIF-8, ZIF67 and ZIF-90). NBO and EDD analyses of the activation step also confirmed the charge redistribution and bending of the CO_2 molecule as it interacts with the catalyst surface. During the protonation step of the carboxylate ion, the values of released energy for ZIF-8, ZIF-67, and ZIF-90 are 9.08 eV, 8.67 eV, and 8.52 eV, indicating the stabilization of the produced carboxyl group. Upon electron-coupled proton transfer, decarboxylation occurs, which releases an energy of 1.03 eV, 1.81 eV, and 2.35 eV, respectively. Overall, this study indicates that the ZIF-8 complex is an effective electrocatalyst for the CO_2RR, which gives researchers a new opportunity to enhance the catalytic potential of ZIF-8 and create a novel electrocatalyst derived from ZIF-8 for effective CO_2RR.

Conflicts of interest

The authors declare that they have no known competing financial interests or personal relationships that could have appeared to influence the work reported in this paper.

Data availability

Data will be made available upon request.

Supplementary information (SI) is available. See DOI: https://doi.org/10.1039/d5ra05431a.

Acknowledgements

The authors are grateful to Dr Sehrish Sarfaraz for her insightful recommendations and unwavering assistance during the research work of this manuscript. The authors are also thankful to the University of the Punjab, Lahore, Pakistan for providing facilities during this work as a host institution.

References

1 S. Chu and A. Majumdar, Opportunities and challenges for a sustainable energy future, *Nature*, 2012, **488**(7411), 294–303.

2 S. J. Davis, K. Caldeira and H. D. Matthews, Future CO_2 emissions and climate change from existing energy infrastructure, *Science*, 2010, **329**(5997), 1330–1333.

3 M. McNutt, Time's up, CO_2, *Science*, 2019, **365**(6452), 411.

4 H. Mikulčić, I. R. Skov, D. F. Dominković, S. R. W. Alwi, Z. A. Manan, R. Tan and X. Wang, Flexible Carbon Capture and Utilization technologies in future energy systems and the utilization pathways of captured CO_2, *Renew. Sustain. Energy Rev.*, 2019, **114**, 109338.

5 Y. Ma, X. Wang, Y. Jia, X. Chen, H. Han and C. Li, Titanium dioxide-based nanomaterials for photocatalytic fuel generations, *Chem. Rev.*, 2014, **114**(19), 9987–10043.

6 P. F. Sui, C. Xu, M. N. Zhu, S. Liu, Q. Liu and J. L. Luo, Interface-Induced Electrocatalytic Enhancement of CO_2-to-Formate Conversion on Heterostructured Bismuth-Based Catalysts, *Small*, 2022, **18**(1), 2105682.

7 J. M. Ali, A. M. Mohammed and Y. S. Mekonnen, Mechanistic study on the coupling reaction of CO_2 with propylene oxide catalyzed by $(CH_3)_4PI\cdot MgCl_2$, *J. Comput. Chem.*, 2022, **43**(14), 961–971.

Open Access Article. Published on 11 December 2025. Downloaded on 4/30/2026 6:26:57 AM.
This article is licensed under a Creative Commons Attribution-NonCommercial 3.0 Unported Licence.

8 C. S. Galik, A continuing need to revisit BECCS and its potential, *Nat. Clim. Change*, 2020, **10**(1), 2–3.

9 S. J. Davis, N. S. Lewis, M. Shaner, S. Aggarwal, D. Arent, I. L. Azevedo and K. Caldeira, Net-zero emissions energy systems, *Science*, 2018, **360**(6396), eaas9793.

10 R. Meys, A. Kätelhön, M. Bachmann, B. Winter, C. Zibunas, S. Suh and A. Bardow, Achieving net-zero greenhouse gas emission plastics by a circular carbon economy, *Science*, 2021, **374**(6563), 71–76.

11 G. D. Fao and J. C. Jiang, Theoretical investigation of CO_2 conversion on corrugated g-C_3N_4 Surface decorated by single-atom of Fe, Co, and Pd, *Mol. Catal.*, 2022, **526**, 112402.

12 F. Raziq, A. Aligayev, H. Shen, S. Ali, R. Shah, S. Ali and L. Qiao, Exceptional photocatalytic activities of rGO modified (B, N) Co-doped WO_3, coupled with CdSe QDs for one photon Z-scheme system: a joint experimental and dft study, *Adv. Sci.*, 2022, **9**(2), 2102530.

13 F. Raziq, K. Khan, S. Ali, S. Ali, H. Xu, I. Ali and L. Qiao, Accelerating CO_2 reduction on novel double perovskite oxide with sulfur, carbon incorporation: synergistic electronic and chemical engineering, *Chem. Eng. J.*, 2022, **446**, 137161.

14 F. Wahid, S. Ali, P. M. Ismail, F. Raziq, S. Ali, J. Yi and L. Qiao, Metal single atom doped 2D materials for photocatalysis: current status and future perspectives, *Prog. Energy*, 2023, **5**, 012001.

15 S. Wang, G. Li, L. Chen, Z. Li, Z. Wu, X. Kong and Z. Liu, The emerging applications of metal phosphides in carbon dioxide reduction reaction, *Funct. Mater. Lett.*, 2021, **14**(07), 2130017.

16 W. Zhang, Y. Hu, L. Ma, G. Zhu, Y. Wang, X. Xue and Z. Jin, Progress and perspective of electrocatalytic CO_2 reduction for renewable carbonaceous fuels and chemicals, *Adv. Sci.*, 2018, **5**(1), 1700275.

17 D. Gao, R. M. Arán-Ais, H. S. Jeon and B. Roldan Cuenya, Rational catalyst and electrolyte design for CO_2 electroreduction towards multicarbon products, *Nat. Catal.*, 2019, **2**(3), 198–210.

18 D. U. Nielsen, X. M. Hu, K. Daasbjerg and T. Skrydstrup, Chemically and electrochemically catalysed conversion of CO_2 to CO with follow-up utilization to value-added chemicals, *Nat. Catal.*, 2018, **1**(4), 244–254.

19 S. Ali, P. M. Ismail, F. Wahid, A. Kumar, M. Haneef, F. Raziq and H. Xu, Benchmarking the two-dimensional conductive $Y_3(C_6X_6)_2$ (Y= Co, Cu, Pd, Pt; X= NH, NHS, S) metal-organic framework nanosheets for CO_2 reduction reaction with tunable performance, *Fuel Process. Technol.*, 2022, **236**, 107427.

20 S. Ali, R. Iqbal, F. Wahid, P. M. Ismail, A. Saleem, S. Ali and L. Qiao, Cobalt coordinated two-dimensional covalent organic framework a sustainable and robust electrocatalyst for selective CO_2 electrochemical conversion to formic acid, *Fuel Process. Technol.*, 2022, **237**, 107451.

21 S. Ali, G. Yasin, R. Iqbal, X. Huang, J. Su, S. Ibraheem and H. Xu, Porous aza-doped graphene-analogous 2D material a unique catalyst for CO_2 conversion to formic-acid by hydrogenation and electroreduction approaches, *Mol. Catal.*, 2022, **524**, 112285.

22 R. Iqbal, M. B. Akbar, A. Ahmad, A. Hussain, N. Altaf, S. Ibraheem and S. Ali, Exploring the Synergistic Effect of Novel Ni-Fe in 2D Bimetallic Metal-Organic Frameworks for Enhanced Electrochemical Reduction of CO_2, *Adv. Mater. Interfaces*, 2022, **9**(1), 2101505.

23 C. Cometto, L. Chen, P. K. Lo, Z. Guo, K. C. Lau, E. Anxolabéhère-Mallart and M. Robert, Highly selective molecular catalysts for the CO_2-to-CO electrochemical conversion at very low overpotential. Contrasting Fe vs. Co quaterpyridine complexes upon mechanistic studies, *ACS Catal.*, 2018, **8**(4), 3411–3417.

24 G. Yun, S. Y. Hwang, J. Y. Maeng, Y. J. Kim, C. K. Rhee and Y. Sohn, Electrochemical CO_2/CO reduction on Ag/Cu electrodes and exploring minor Fischer–Tropsch reaction pathways, *Appl. Surf. Sci.*, 2024, **649**, 159179.

25 B. Hu, C. Guild and S. L. Suib, Thermal, electrochemical, and photochemical conversion of CO_2 to fuels and value-added products, *J. CO2 Util.*, 2013, **1**, 18–27.

26 Y. Zhou, R. Zhou, X. Zhu, N. Han, B. Song, T. Liu and Y. Li, Mesoporous PdAg nanospheres for stable electrochemical CO_2 reduction to formate, *Adv. Mater.*, 2020, **32**(30), 2000992.

27 P. Su, W. Xu, Y. Qiu, T. Zhang, X. Li and H. Zhang, Ultrathin bismuth nanosheets as a highly efficient CO_2 reduction electrocatalyst, *ChemSusChem*, 2018, **11**(5), 848–853.

28 C. Costentin, S. Drouet, G. Passard, M. Robert and J. M. Savéant, Proton-coupled electron transfer cleavage of heavy-atom bonds in electrocatalytic processes. Cleavage of a C–O bond in the catalyzed electrochemical reduction of CO_2, *J. Am. Chem. Soc.*, 2013, **135**(24), 9023–9031.

29 C. Yang, J. Chai, Z. Wang, Y. Xing, J. Peng and Q. Yan, Recent progress on bismuth-based nanomaterials for electrocatalytic carbon dioxide reduction, *Chem. Res. Chin. Univ.*, 2020, **36**(3), 410–419.

30 M. T. Tang, H. Peng, P. S. Lamoureux, M. Bajdich and F. Abild-Pedersen, From electricity to fuels: descriptors for C1 selectivity in electrochemical CO_2 reduction, *Appl. Catal., B*, 2020, **279**, 119384.

31 D. Y. Jo, H. C. Ham and K. Y. Lee, Facet-dependent electrocatalysis in the HCOOH synthesis from CO_2 reduction on Cu catalyst: a density functional theory study, *Appl. Surf. Sci.*, 2020, **527**, 146857.

32 Z. Li, D. He, X. Yan, S. Dai, S. Younan, Z. Ke and J. Gu, Size-dependent nickel-based electrocatalysts for selective CO_2 reduction, *Angew. Chem.*, 2020, **132**(42), 18731–18736.

33 Y. Li, Z. Tian and L. Chen, Theoretical understanding of the interface effect in promoting electrochemical CO_2 reduction on Cu–Pd alloys, *J. Phys. Chem. C*, 2021, **125**(39), 21381–21389.

34 T. M. Suzuki, T. Ishizaki, S. Kosaka, N. Takahashi, N. Isomura, J. Seki and T. Morikawa, Electrochemical CO_2 reduction over nanoparticles derived from an oxidized Cu–Ni intermetallic alloy, *Chem. Commun.*, 2020, **56**(95), 15008–15011.

© 2025 The Author(s). Published by the Royal Society of Chemistry

Open Access Article. Published on 11 December 2025. Downloaded on 4/30/2026 6:26:57 AM.
This article is licensed under a Creative Commons Attribution-NonCommercial 3.0 Unported Licence.

35 Y. Xu, C. Li, Y. Xiao, C. Wu, Y. Li, Y. Li and J. He, Tuning the selectivity of liquid products of CO_2RR by Cu–Ag alloying, *ACS Appl. Mater. Interfaces*, 2022, **14**(9), 11567–11574.

36 N. Kumar, N. Seriani and R. Gebauer, DFT insights into electrocatalytic CO_2 reduction to methanol on α-Fe_2O_3 (0001) surfaces, *Phys. Chem. Chem. Phys.*, 2020, **22**(19), 10819–10827.

37 B. Liu, X. Yao, Z. Zhang, C. Li, J. Zhang, P. Wang and C. Zhao, Synthesis of Cu_2O nanostructures with tunable crystal facets for electrochemical CO_2 reduction to alcohols, *ACS Appl. Mater. Interfaces*, 2021, **13**(33), 39165–39177.

38 F. Y. Gao, Z. Z. Wu and M. R. Gao, Electrochemical CO_2 reduction on transition-metal chalcogenide catalysts: recent advances and future perspectives, *Energy Fuels*, 2021, **35**(16), 12869–12883.

39 X. Shao, X. Zhang, Y. Liu, J. Qiao, X. D. Zhou, N. Xu and J. Zhang, Metal chalcogenide-associated catalysts enabling CO_2 electroreduction to produce low-carbon fuels for energy storage and emission reduction: catalyst structure, morphology, performance, and mechanism, *J. Mater. Chem. A*, 2021, **9**(5), 2526–2559.

40 T. Asset, S. T. Garcia, S. Herrera, N. Andersen, Y. Chen, E. J. Peterson and P. Atanassov, Investigating the nature of the active sites for the CO_2 reduction reaction on carbon-based electrocatalysts, *ACS Catal.*, 2019, **9**(9), 7668–7678.

41 S. Fu, X. Liu, J. Ran, Y. Jiao and S. Z. Qiao, CO_2 reduction by single copper atom supported on g-C_3N_4 with asymmetrical active sites, *Appl. Surf. Sci.*, 2021, **540**, 148293.

42 C. Zhang, S. Yang, J. Wu, M. Liu, S. Yazdi, M. Ren and J. M. Tour, Electrochemical CO_2 reduction with atomic iron-dispersed on nitrogen-doped graphene, *Adv. Energy Mater.*, 2018, **8**(19), 1703487.

43 Z. Feng, Y. Tang, Y. Ma, Y. Li, Y. Dai, H. Ding and X. Dai, Theoretical investigation of CO_2 electroreduction on N (B)-doped graphdiyne mononlayer supported single copper atom, *Appl. Surf. Sci.*, 2021, **538**, 148145.

44 Z. Feng, G. Su, H. Ding, Y. Ma, Y. Li, Y. Tang and X. Dai, Atomic alkali metal anchoring on graphdiyne as single-atom catalysts for capture and conversion of CO_2 to HCOOH, *Mol. Catal.*, 2020, **494**, 111142.

45 Z. Feng, Y. Tang, Y. Ma, Y. Li, Y. Dai, W. Chen and X. Dai, Theoretical computation of the electrocatalytic performance of CO_2 reduction and hydrogen evolution reactions on graphdiyne monolayer supported precise number of copper atoms, *Int. J. Hydrogen Energy*, 2021, **46**(7), 5378–5389.

46 Y. Wang, J. Liu, Y. Wang, A. M. Al-Enizi and G. Zheng, Tuning of CO_2 reduction selectivity on metal electrocatalysts, *Small*, 2017, **13**(43), 1701809.

47 M. Cho, J. M. Kim, B. Kim, S. Yim, Y. J. Kim, Y. S. Jung and J. Oh, Versatile, transferrable 3-dimensionally nanofabricated Au catalysts with high-index crystal planes for highly efficient and robust electrochemical CO_2 reduction, *J. Mater. Chem. A*, 2019, **7**(11), 6045–6052.

48 Y. Zhao, C. Wang, Y. Liu, D. R. MacFarlane and G. G. Wallace, Engineering surface amine modifiers of ultrasmall gold nanoparticles supported on reduced graphene oxide for improved electrochemical CO_2 reduction, *Adv. Energy Mater.*, 2018, **8**(25), 1801400.

49 S. Zhao, Z. Tang, S. Guo, M. Han, C. Zhu, Y. Zhou and Z. Kang, Enhanced activity for CO_2 electroreduction on a highly active and stable ternary Au-C Dots-C_3N_4 electrocatalyst, *ACS Catal.*, 2018, **8**(1), 188–197.

50 Y. Zhang, L. Hu and W. Han, Insights into in situ one-step synthesis of carbon-supported nano-particulate gold-based catalysts for efficient electrocatalytic CO_2 reduction, *J. Mater. Chem. A*, 2018, **6**(46), 23610–23620.

51 J. Kim, J. T. Song, H. Ryoo, J. G. Kim, S. Y. Chung and J. Oh, Morphology-controlled Au nanostructures for efficient and selective electrochemical CO_2 reduction, *J. Mater. Chem. A*, 2018, **6**(12), 5119–5128.

52 H. Q. Fu, L. Zhang, L. R. Zheng, P. F. Liu, H. Zhao and H. G. Yang, Enhanced CO_2 electroreduction performance over Cl-modified metal catalysts, *J. Mater. Chem. A*, 2019, **7**(20), 12420–12425.

53 A. Seifitokaldani, Switching between CO_2 Electroreduction Pathways. in *Electrochemical Society Meeting Abstracts*, The Electrochemical Society, Inc., 2019, vol. 235, 31, pp. 1588.

54 J. Wang, S. Kattel, C. J. Hawxhurst, J. H. Lee, B. M. Tackett, K. Chang and J. G. Chen, Enhancing activity and reducing cost for electrochemical reduction of CO_2 by supporting palladium on metal carbides, *Angew. Chem., Int. Ed.*, 2019, **58**(19), 6271–6275.

55 H. Cui, Y. Guo, L. Guo, L. Wang, Z. Zhou and Z. Peng, Heteroatom-doped carbon materials and their composites as electrocatalysts for CO_2 reduction, *J. Mater. Chem. A*, 2018, **6**(39), 18782–18793.

56 A. S. Varela, W. Ju and P. Strasser, Molecular nitrogen–carbon catalysts, solid metal organic framework catalysts, and solid metal/nitrogen-doped carbon (MNC) catalysts for the electrochemical CO_2 reduction, *Adv. Energy Mater.*, 2018, **8**(30), 1703614.

57 A. Vasileff, Y. Zheng and S. Z. Qiao, Carbon solving carbon's problems: recent progress of nanostructured carbon-based catalysts for the electrochemical reduction of CO_2, *Adv. Energy Mater.*, 2017, **7**(21), 1700759.

58 X. Duan, J. Xu, Z. Wei, J. Ma, S. Guo, S. Wang and S. Dou, Metal-free carbon materials for CO_2 electrochemical reduction, *Adv. Mater.*, 2017, **29**(41), 1701784.

59 X. Wang, Z. Chen, X. Zhao, T. Yao, W. Chen, R. You and Y. Li, Regulation of coordination number over single Co sites: triggering the efficient electroreduction of CO2, *Angew. Chem.*, 2018, **130**(7), 1962–1966.

60 C. Yan, H. Li, Y. Ye, H. Wu, F. Cai, R. Si and X. Bao, Coordinatively unsaturated nickel–nitrogen sites towards selective and high-rate CO_2 electroreduction, *Energy Environ. Sci.*, 2018, **11**(5), 1204–1210.

61 H. B. Yang, S. F. Hung, S. Liu, K. Yuan, S. Miao, L. Zhang and B. Liu, Atomically dispersed Ni (I) as the active site for electrochemical CO_2 reduction, *Nat. Energy*, 2018, **3**(2), 140–147.

62 W. Ren, X. Tan, W. Yang, C. Jia, S. Xu, K. Wang and C. Zhao, Isolated diatomic Ni-Fe metal–nitrogen sites for synergistic

Open Access Article. Published on 11 December 2025. Downloaded on 4/30/2026 6:26:57 AM. This article is licensed under a Creative Commons Attribution-NonCommercial 3.0 Unported Licence.

electroreduction of CO_2, *Angew. Chem., Int. Ed.*, 2019, **58**(21), 6972–6976.

63 G. Singh, J. Lee, A. Karakoti, R. Bahadur, J. Yi, D. Zhao and A. Vinu, Emerging trends in porous materials for CO_2 capture and conversion, *Chem. Soc. Rev.*, 2020, **49**(13), 4360–4404.

64 X. Wang, Y. Zou, Y. Zhang, B. Marchetti, Y. Liu, J. Yi and J. Zhang, Tin-based metal organic framework catalysts for high-efficiency electrocatalytic CO_2 conversion into formate, *J. Colloid Interface Sci.*, 2022, **626**, 836–847.

65 T. Najam, S. S. A. Shah, M. S. Bashir, and A. U. Rehman, Covalent Organic Framework-Based Electrocatalysts for CO_2 Reduction Reaction. in *Noble Metal-Free Electrocatalysts: Fundamentals and Recent Advances in Electrocatalysts for Energy Applications*, American Chemical Society, 2022, vol 1, pp. 257–274.

66 Y. Zheng, A. Vasileff, X. Zhou, Y. Jiao, M. Jaroniec and S. Z. Qiao, Understanding the roadmap for electrochemical reduction of CO_2 to multi-carbon oxygenates and hydrocarbons on copper-based catalysts, *J. Am. Chem. Soc.*, 2019, **141**(19), 7646–7659.

67 V. H. Nguyen, B. S. Nguyen, Z. Jin, M. Shokouhimehr, H. W. Jang, C. Hu and Q. Van Le, Towards artificial photosynthesis: Sustainable hydrogen utilization for photocatalytic reduction of CO_2 to high-value renewable fuels, *Chem. Eng. J.*, 2020, **402**, 126184.

68 T. P. Nguyen, D. L. T. Nguyen, V. H. Nguyen, T. H. Le, D. V. N. Vo, Q. T. Trinh and Q. V. Le, Recent advances in TiO_2-based photocatalysts for reduction of CO_2 to fuels, *Nanomaterials*, 2020, **10**(2), 337.

69 Y. Wang, P. Hou, Z. Wang and P. Kang, Zinc imidazolate metal–organic frameworks (ZIF-8) for electrochemical reduction of CO_2 to CO, *ChemPhysChem*, 2017, **18**(22), 3142–3147.

70 X. Jiang, H. Li, J. Xiao, D. Gao, R. Si, F. Yang and X. Bao, Carbon dioxide electroreduction over imidazolate ligands coordinated with Zn (II) center in ZIFs, *Nano Energy*, 2018, **52**, 345–350.

71 S. Dou, J. Song, S. Xi, Y. Du, J. Wang, Z. F. Huang and X. Wang, Boosting electrochemical CO_2 reduction on metal–organic frameworks via ligand doping, *Angew. Chem., Int. Ed.*, 2019, **58**(12), 4041–4045.

72 J. Cao, S. Sun, X. Li, Z. Yang, W. Xiong, Y. Wu and Y. Zhang, Efficient charge transfer in aluminum-cobalt layered double hydroxide derived from Co-ZIF for enhanced catalytic degradation of tetracycline through peroxymonosulfate activation, *Chem. Eng. J.*, 2020, **382**, 122802.

73 I. S. Flyagina, E. M. Mahdi, K. Titov and J. C. Tan, Thermo-mechanical properties of mixed-matrix membranes encompassing zeolitic imidazolate framework-90 and polyvinylidine difluoride: ZIF-90/PVDF nanocomposites, *APL Mater.*, 2017, **5**(8), 086104.

74 X. G. TIAN, Y. ZHANG and T. S. YANG, First-principles study of H2 dissociative adsorption reactions on WO_3 surfaces, *Acta Phys.-Chim. Sin.*, 2012, **28**(5), 1063–1069.

75 A. A. Latimer, A. R. Kulkarni, H. Aljama, J. H. Montoya, J. S. Yoo, C. Tsai and J. K. Nørskov, Understanding trends in C–H bond activation in heterogeneous catalysis, *Nat. Mater.*, 2017, **16**(2), 225–229.

76 Z. F. Huang, J. Song, Y. Du, S. Xi, S. Dou, J. M. V. Nsanzimana and X. Wang, Chemical and structural origin of lattice oxygen oxidation in Co–Zn oxyhydroxide oxygen evolution electrocatalysts, *Nat. Energy*, 2019, **4**(4), 329–338.

77 M. Frisch, F. Clemente, G. Trucks, H. Schlegel, G. Scuseria, M. Robb, J. Cheeseman, G. Scalmani, V. Barone, B. Mennucci, G. A. Petersson, H. Nakatsuji, M. Caricato, X. Li, H. P. Hratchian, A. F. Izmaylov, J. Bloino, G. Zhe, *Gaussian 09, Revision a. 01*, 2009, pp. 20–44.

78 H. Tahir, N. Kosar, K. Ayub and T. Mahmood, Outstanding NLO response of thermodynamically stable single and multiple alkaline earth metals doped C_{20} fullerene, *J. Mol. Liq.*, 2020, **305**, 112875.

79 R. Ahmadi and S. Pourkarim, Investigation of fullerene (C), *Int. J. Bio-Inorg. Hybr. Nanomater.*, 2015, **4**(4), 249–254.

80 S. Osuna, M. Swart and M. Sola, Dispersion corrections essential for the study of chemical reactivity in fullerenes, *J. Phys. Chem.*, 2011, **115**(15), 3491–3496.

81 M. T. Baei, A. A. Peyghan, Z. Bagheri and M. B. Tabar, B-doping makes the carbon nanocones sensitive towards NO molecules, *Phys. Lett. A*, 2012, **377**(1–2), 107–111.

82 S. F. Rastegar, A. A. Peyghan and H. Soleymanabadi, Ab initio studies of the interaction of formaldehyde with beryllium oxide nanotube, *Phys. E Low-dimens. Syst. Nanostruct.*, 2015, **68**, 22–27.

83 A. A. Peyghan, H. Soleymanabadi and M. Moradi, Structural and electronic properties of pyrrolidine-functionalized [60] fullerenes, *J. Phys. Chem. Solids*, 2013, **74**(11), 1594–1598.

84 S. Sarfaraz, M. Yar, M. Ans, M. A. Gilani, R. Ludwig, M. A. Hashmi and K. Ayub, Computational investigation of a covalent triazine framework (CTF-0) as an efficient electrochemical sensor, *RSC Adv.*, 2022, **12**(7), 3909–3923.

85 S. Sarfaraz, M. Yar and K. Ayub, Covalent triazine framework (CTF-0) surface as a smart sensing material for the detection of CWAs and industrial pollutants, *Mater. Sci. Semicond. Process.*, 2022, **139**, 106334.

86 S. Sarfaraz, M. Yar, A. A. Khan, R. Ahmad and K. Ayub, DFT investigation of adsorption of nitro-explosives over C2N surface: Highly selective towards trinitro benzene, *J. Mol. Liq.*, 2022, **352**, 118652.

87 X. Sun, M. Keywanlu and R. Tayebee, Experimental and molecular dynamics simulation study on the delivery of some common drugs by ZIF-67, ZIF-90, and ZIF-8 zeolitic imidazolate frameworks, *Appl. Organomet. Chem.*, 2021, **35**(11), e6377.

88 P. Saha, S. Amanullah and A. Dey, Selectivity in electrochemical CO_2 reduction, *Acc. Chem. Res.*, 2022, **55**(2), 134–144.

89 G. M. Tomboc, S. Choi, T. Kwon, Y. J. Hwang and K. Lee, Potential link between Cu surface and selective CO_2 electroreduction: perspective on future electrocatalyst designs, *Adv. Mater.*, 2020, **32**(17), 1908398.

90 F. Y. Gao, R. C. Bao, M. R. Gao and S. H. Yu, Electrochemical CO_2-to-CO conversion: electrocatalysts, electrolytes, and electrolyzers, *J. Mater. Chem. A*, 2020, **8**(31), 15458–15478.

© 2025 The Author(s). Published by the Royal Society of Chemistry

Open Access Article. Published on 11 December 2025. Downloaded on 4/30/2026 6:26:57 AM.
This article is licensed under a Creative Commons Attribution-NonCommercial 3.0 Unported Licence.

91 J. H. Cho, C. Lee, S. H. Hong, H. Y. Jang, S. Back, M. G. Seo and S. Y. Kim, Transition metal ion doping on ZIF-8 enhances the electrochemical CO_2 reduction reaction, *Adv. Mater.*, 2023, **35**(43), 2208224.

92 S. G. Lias, J. F. Liebman and R. D. Levin, Evaluated gas phase basicities and proton affinities of molecules; heats of formation of protonated molecules, *J. Phys. Chem. Ref. Data*, 1984, **13**(3), 695–808.

93 Y. Hu, L. Gao, Z. Dai, G. Sun, T. Zhang, S. Jia and X. Zhang, DFT investigation on the decarboxylation mechanism of ortho hydroxy benzoic acids with acid catalysis, *J. Mol. Model.*, 2016, **22**(3), 56.

94 A. Seifitokaldani, C. M. Gabardo, T. Burdyny, C. T. Dinh, J. P. Edwards, M. G. Kibria and E. H. Sargent, Hydronium-induced switching between CO_2 electroreduction pathways, *J. Am. Chem. Soc.*, 2018, **140**(11), 3833–3837.

95 J. Jiao, R. Lin, S. Liu, W. C. Cheong, C. Zhang, Z. Chen and Y. Li, Copper atom-pair catalyst anchored on alloy nanowires for selective and efficient electrochemical reduction of CO_2, *Nat. Chem.*, 2019, **11**(3), 222–228.

96 M. Zheng, X. Zhou, Y. Zhou and M. Li, Theoretical insights into mechanisms of electrochemical reduction of CO_2 to ethylene catalyzed by Pd3Au, *Appl. Surf. Sci.*, 2022, **572**, 151474.

97 Y. S. Al-Faiyz, S. Sarfaraz, M. Yar, S. Munsif, A. A. Khan, B. Amin and K. Ayub, Efficient detection of nerve agents through carbon nitride quantum dots: a DFT approach, *Nanomaterials*, 2023, **13**(2), 251.

98 A. Mukhtar, S. Sarfaraz and K. Ayub, Organic transformations in the confined space of porous organic cage CC_2; catalysis or inhibition, *RSC Adv.*, 2022, **12**(37), 24397–24411.

99 M. Asif, S. Sarfaraz and K. Ayub, DFT investigation of M2F superalkali doped dodecafluorophenylene ($C_{13}H_{10}F_{12}$) derivatives with remarkable static and dynamic NLO response, *Phys. Scr.*, 2024, **99**(6), 065108.

© 2025 The Author(s). Published by the Royal Society of Chemistry